A-Site and B-Site Charge Orderings in an s−d Level Controlled Perovskite Oxide PbCoO₃

Yuki Sakai,[†] Junye Yang,[‡,◀] Runze Yu,[§,◆] Hajime Hojo,[§,◇] Ikuya Yamada,[∥] Ping Miao,[⊥,∞] Sanghyun Lee,[⊥] Shuki Torii,[⊥] Takashi Kamiyama,[⊥,#] Marjana Ležaić,[▽] Gustav Bihlmayer,[▽] Masaichiro Mizumaki,[¶] Jun Komiyama,[⊗] Takashi Mizokawa,[□] Hajime Yamamoto,[§] Takumi Nishikubo,[§] Yuichiro Hattori,[§] Kengo Oka,[■] Yunyu Yin,[‡] Jianhong Dai,[‡] Wenmin Li,[‡] Shigenori Ueda,[○,●] Akihisa Aimi,[△,⬡] Daisuke Mori,[△] Yoshiyuki Inaguma,[△] Zhiwei Hu,[▲] Takayuki Uozumi,[▼] Changqing Jin,[‡,○,⊕] Youwen Long,*[,‡,○] and Masaki Azuma*[,§]

[†]Kanagawa Academy of Science and Technology, KSP, 3-2-1 Sakado, Takatsu-ku, Kawasaki City, Kanagawa 213-0012, Japan
[‡]Beijing National Laboratory for Condensed Matter Physics, Institute of Physics, Chinese Academy of Sciences, Beijing 100190, China
[§]Laboratory for Materials and Structures, Tokyo Institute of Technology, 4259 Nagatsuta, Midori, Yokohama 226-8503, Japan
[∥]Nanoscience and Nanotechnology Research Center, Osaka Prefecture University, 1-2 Gakuen-cho, Naka-ku, Sakai, Osaka 599-8570, Japan
[⊥]Institute of Materials Structure Science (IMSS), High Energy Accelerator Research Organization (KEK), 203-1, Tokai-mura, Ibaraki 319-1106, Japan
[#]Department of Materials Structure Science, School of High Energy Accelerator Science, SOKENDAI (The Graduate University for Advanced Studies), 203-1, Tokai-mura, Ibaraki 319-1106, Japan
[▽]Peter Grünberg Institut and Institute for Advanced Simulation, Forschungszentrum Jülich and JARA, Jülich 52425, Germany
[¶]Japan Synchrotron Radiation Research Institute, SPring-8, Sayo-gun, Hyogo 679-5198, Japan
[⊗]Department of Complexity Science and Engineering, University of Tokyo, 5-1-5 Kashiwanoha, Kashiwa, Chiba 277-8561, Japan
[□]Department of Applied Physics, School of Advanced Science and Engineering, Waseda University, 3-4-1 Okubo, Shinjuku-ku, Tokyo 169-8555, Japan
[■]Department of Applied Chemistry, Faculty of Science and Engineering, Chuo University, 1-13-27 Kasuga, Bunkyo-ku, Tokyo 112-8551, Japan
[○]Quantum Beam Unit, National Institute for Materials Science, Sengen, Tsukuba 305-0047, Japan
[●]Synchrotron X-ray Station at SPring-8, National Institute for Materials Science, Sayo, Hyogo 679-5148, Japan
[△]Department of Chemistry, Faculty of Science, Gakushuin University, 1-5-1 Mejiro, Toshima-ku, Tokyo 171-8588, Japan
[▲]Max-Planck Institute for Chemical Physics of Solids, Nöthnitzer Straße 40, 01187 Dresden, Germany
[▼]Graduate School of Engineering, Osaka Prefecture University, 1-1 Gakuen-cho, Sakai, Osaka 599-8531, Japan
[○]Collaborative Innovation Center of Quantum Matter, University of Chinese Academy of Sciences, Beijing 100190, China
[⊕]School of Physical Sciences, University of Chinese Academy of Sciences, Beijing 100190, China

S Supporting Information

ABSTRACT: Perovskite PbCoO₃ synthesized at 12 GPa was found to have an unusual charge distribution of $Pb^{2+}Pb^{4+}_3Co^{2+}_2Co^{3+}_2O_{12}$ with charge orderings in both the A and B sites of perovskite ABO_3. Comprehensive studies using density functional theory (DFT) calculation, electron diffraction (ED), synchrotron X-ray diffraction (SXRD), neutron powder diffraction (NPD), hard X-ray photoemission spectroscopy (HAXPES), soft X-ray absorption spectroscopy (XAS), and measurements of specific heat as well as magnetic and electrical properties provide evidence of lead ion and cobalt ion charge ordering leading to $Pb^{2+}Pb^{4+}_3Co^{2+}_2Co^{3+}_2O_{12}$ quadruple perovskite structure. It is shown that the average valence distribution of $Pb^{3.5+}Co^{2.5+}O_3$ between $Pb^{3+}Cr^{3+}O_3$ and $Pb^{4+}Ni^{2+}O_3$ can be stabilized by tuning the energy levels of Pb 6s and transition metal 3d orbitals.
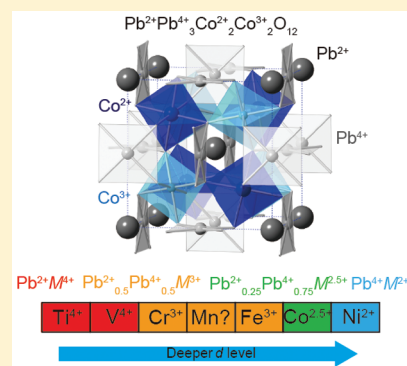
1. INTRODUCTION

Charge degree of freedom in transition metals gives rise to various fascinating properties such as charge ordering associated with metal−insulator transition,[1−6] high-temperature (HT) super-conductivity,[1,7,8] colossal magnetoresistance[1,9] and high thermo-power.[10] Changes in the oxidation state of Mn even play a crucial role in photosynthesis,[11] while in redox-based resistive random access memory (ReRAM) valence changes of the transition-metal ions lie behind the changes of the resistance of the device.[12] Metal ions with half-integer valence tend to split into two integer valence ions, and these get spatially ordered as typically observed in $La_{0.5}Ca_{0.5}Mn^{3.5+}O_3$.[1,2] To realize a half-integer valence state and charge ordering in the B site of a perovskite ABO_3, it is generally necessary to mix two or more elements with different valences in the A site.[3] In this report we show that charge orderings in both the A and B sites of perovskite ABO_3 can be stabilized by tuning the energy levels of Pb $6s$ and transition metal $3d$ orbitals.

Bi and Pb are main-group elements, but they have charge degree of freedom stemming from the possibility of having either the $6s^2$ (Bi^{3+}, Pb^{2+}) or the $6s^0$ (Bi^{5+}, Pb^{4+}) electronic configurations, typically found in $BaBiO_3$ ($BaBi^{3+}_{0.5}Bi^{5+}_{0.5}O_3$).[13] They are called valence-skipping (or negative-U) ions because the $6s^1$ configurations (Bi^{4+}, Pb^{3+}) are prohibited.[14] This characteristic of Pb is utilized in lead-acid batteries.[15] Since the $6s$ states of these elements are close to the d levels of transition metals and the oxygen $2p$ level, $BiMO_3$ and $PbMO_3$ exhibit systematic valence distribution changes with changes in the $3d$ transition metal M. From left to right in the periodic table, $BiCrO_3$ through $BiCoO_3$ are all $Bi^{3+}M^{3+}O_3$[16] but $BiNiO_3$ has the unusual valence state $Bi^{3+}_{0.5}Bi^{5+}_{0.5}Ni^{2+}O_3$.[17] Temperature-induced intermetallic charge transfer accompanied by negative thermal expansion is observed for $Bi_{1−x}Ln_xNiO_3$ (Ln: lanthanides)[18,19] and $BiNi_{1−x}Fe_xO_3$.[20] Similar charge distribution change is observed twice in $PbMO_3$ depending on the depth of the $3d$ level of the transition metal: $PbTiO_3$ and $PbVO_3$[21] are $Pb^{2+}Ti^{4+}O_3$ and $Pb^{2+}V^{4+}O_3$, $PbCrO_3$[22] is $Pb^{2+}_{0.5}Pb^{4+}_{0.5}Cr^{3+}O_3$ with charge disproportionated Pb^{2+} and Pb^{4+}, and $PbNiO_3$[23] is $Pb^{4+}Ni^{2+}O_3$. This trend indicates that we can control the energy difference between Pb $6s$ and M $3d$ levels by changing the transition metal. The compounds between $PbCrO_3$ and $PbNiO_3$ are not completely explored, and we expected that the unusual half-integer average charge system $Pb^{3.5+}M^{2.5+}O_3$ with charge ordering in both the A and B sites of a perovskite would be found among these compounds. We focused our attention on $PbCoO_3$, which used to be a "missing piece" in $PbMO_3$ family. Despite the extensive investigations of Pb-$3d$ transition metal perovskites as candidate multiferroics, perovskite $PbCoO_3$ had not been obtained previously because synthesis at a pressure above 12 GPa is essential. Perovskite $PbCoO_3$ synthesized at 12 GPa has an unusual charge distribution of $Pb^{2+}Pb^{4+}_3Co^{2+}_2Co^{3+}_2O_{12}$ with charge orderings in both of A and B sites (average charge distribution of $Pb^{3.5+}Co^{2.5+}O_3$). Comprehensive studies using density functional theory (DFT) calculation, electron diffraction (ED), synchrotron X-ray diffraction (SXRD), neutron powder diffraction (NPD), hard X-ray photoemission spectroscopy (HAXPES), soft X-ray absorption spectroscopy (XAS), and measurements of specific heat as well as magnetic and electrical properties provide evidence of lead ion and cobalt ion charge ordering leading to quadruple perovskite structure. The present results offer a much needed new strategy to realizing mixed valence states (possibly of multiple ions) in single-phase oxides and thus open an avenue to the production of next-generation materials with exotic properties such as superconductivity, colossal magnetoresistance, and high thermopower.

2. METHODS SECTION

Polycrystalline samples of $PbCoO_3$ were prepared at 12 GPa as follows. Stoichiometric mixtures of PbO, PbO_2, and Co_3O_4 were sealed in gold capsules and then held at 12 GPa and 1473 K for 30 min in a Kawai-type apparatus. When we tried to make it at 6 GPa, the product was an oxygen-deficient pyrochlore phase (to be reported elsewhere). Our attempt to convert this phase into perovskite by heat treatment at 12 GPa was not successful. It was necessary to start from the mixture of PbO, PbO_2 and Co_3O_4. In addition, the temperature window was quite narrow: the reaction was incomplete when the temperature was too low, and the product reacted with the container when the temperature was too high.

SXRD patterns were collected using a large Debye−Scherrer camera installed at the BL02B2 beamline of SPring-8 and were analyzed using RIETAN-FP programs.[24] The wavelength was 0.41955 Å. NPD patterns were collected with time-of-flight diffractometers installed at Super HRPD (BL08) at the Material and Life Science Experimental Facility (MLF) of the Japan Proton Accelerator Research Complex (J-PARC) and were analyzed using Z-Rietveld.[25,26] A vanadium cell 5.8 mm in diameter was used, and sample was sealed with an indium ring under Ar or He atmospheres. ED patterns of samples at 298 K were obtained using a JEOL JEM-2100F transmission electron microscopy equipped with a double-tilting holder.

Pb-$4f$ HAXPES measurements were made at 300 K with E = 5950 eV at the undulator beamline BL15XU of SPring-8.[27,28] A hemispherical photoelectron analyzer (VG Scienta, R4000) were used in these measurements. The polycrystalline samples used in the HAXPES measurements were fractured in situ. The binding energies were calibrated using the Au $4f_{7/2}$ peak (84.0 eV) and the Fermi edge of gold reference samples. Total energy resolution was set to 240 meV at E = 5953 eV.

The Co-$L_{2,3}$ XAS spectrum was recorded at the 08B beamline of the National Synchrotron Radiation Research Center (NSRRC) in Taiwan using the total-electron-yield mode. The spectrum of a single-crystal CoO sample was measured simultaneously to serve as an absolute energy reference. Clean sample surfaces were obtained by cleaving pelletized samples in situ in an ultrahigh-vacuum chamber with a pressure in the $10^{−10}$ mbar range.

Electrical resistivity was measured by a pseudo 4-probe method. The temperature dependence of the magnetic susceptibility of $PbCoO_3$ was evaluated using the susceptibility measured with a SQUID magneto-meter (Quantum Design, MPMS 5) in an external magnetic field of 1 kOe. The specific heat data were collected using a physical property measurement system (Quantum Design, PPMS-9T).

The structural optimization was based on first-principles density-functional calculations made with the Vienna ab initio simulation package (VASP)[29] and the PAW potentials.[30] The hybrid functional HSE06[31] was used with the mixing factor α = 0.15, which was previously found to yield reasonable results for a set of perovskites containing $3d$-transition elements.[32] In order to compare the theoretically obtained and the experimentally observed structures, we fully relaxed a ferro-magnetic unit cell containing 40 atoms ($2 \times 2 \times 2$ simple perovskite unit cells) within several symmetry constraints. Relaxations with accuracies up to 0.01 eV/Å were carried out with a plane-wave cutoff of 500 eV and a $4 \times 4 \times 4$ Γ-centered k-points mesh (corresponding to an $8 \times 8 \times 8$ mesh in the simple perovskite unit cell). In order to investigate the core level shifts, we used the all-electron FLEUR code[33] based on the full-potential linearized augmented planewave method. Here a $3 \times 3 \times 3$ Γ-centered k-points mesh (corresponding to a $6 \times 6 \times 6$ mesh in the simple perovskite unit cell) and a LAPW basis cutoff parameter k_{max} = 4.2 bohr$^{−1}$ were used. A generalized gradient approximation (GGA)-based exchange and correlation functional (PBE)[34] was used in conjunction with the DFT+U approach with a U_{eff} = 5.9 eV. This value reproduces the difference in the core level positions of Pb^{2+} and Pb^{4+} cations obtained in our calculations with the HSE06 functional in VASP (0.52 eV with GGA+U vs 0.59 eV
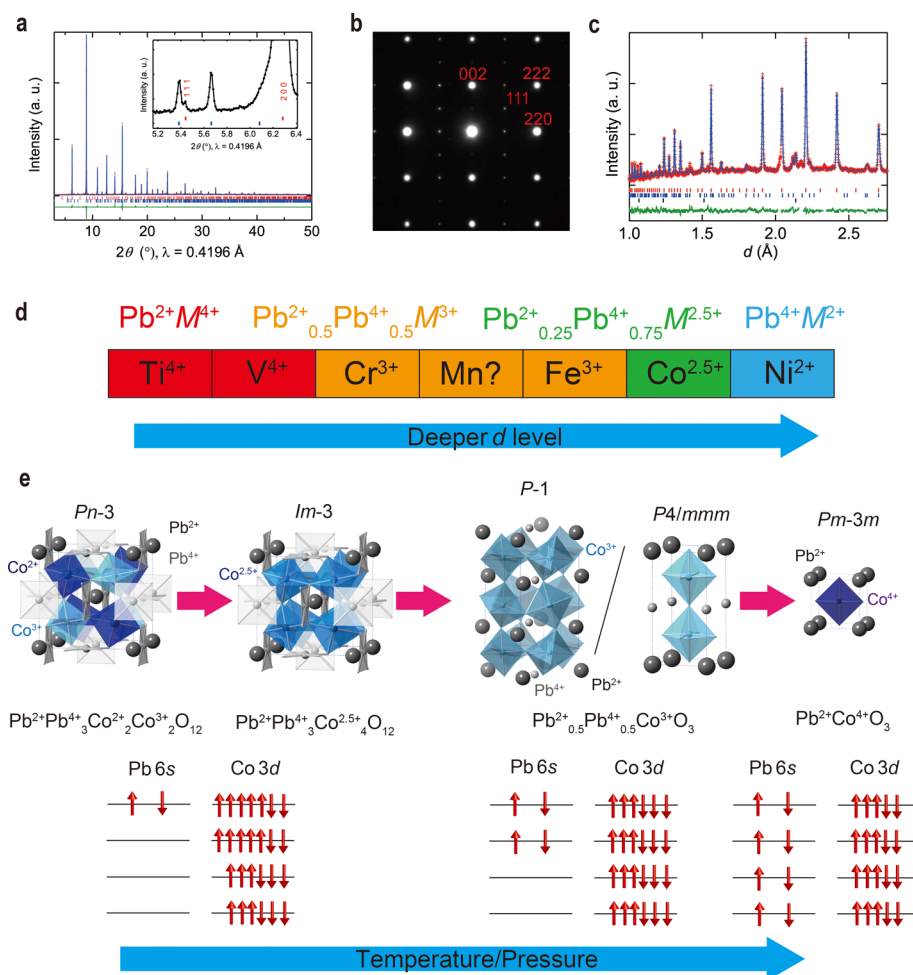
Figure 1. SXRD, ED, and NPD patterns indicating $Pb^{2+}Pb^{4+}_3Co^{2+}_2Co^{3+}_2O_{12}$ superstructure and valence distribution changes depending on composition and condition. (a) Observed (red points), calculated (blue line), and difference (green line) patterns from the Rietveld analysis of the SXRD data at RT. The tick marks correspond to the positions of Bragg reflections of the $Pn\bar{3}$ cubic phase (red) and $Pb_3(CO_3)_2(OH)_2$ (blue). Anisotropic atomic displacement parameters of A'-site: $U_{11} = 1.76(8) \times 10^{-2}$ Å^2, $U_{22} = 6.40(9) \times 10^{-2}$ Å^2, $U_{33} = 0.86(6) \times 10^{-2}$ Å^2. R values (%): $R_{wp} = 5.09$, $R_B = 3.85$, $S = 2.83$. Inset shows the magnified view of SXRD. (111) super lattice reflection which is characteristic for $Pn\bar{3}$ structure is observed. (b) ED patterns along the [011] pseudocubic zone axis at RT. The unit cell is $2a \times 2a \times 2a$, where a represents the lattice parameter of the ideal cubic perovskite structure ($Pm\bar{3}m$). ED patterns along the [001] and [111] pseudocubic zone axis at RT are summarized in Figure S1. (c) Observed (red points), calculated (blue line), and difference (green line) patterns from the Rietveld analysis of the NPD data at RT. The tick marks correspond to the positions of Bragg reflections of the $Pn\bar{3}$ cubic phase (red), a $Pb_3(CO_3)_2(OH)_2$ impurity (blue), and the vanadium cell (black). The data in the ranges without the difference plot were excluded in the refinement because of the presence of reflections from unidentified impurities. (111) super lattice reflection which is characteristic for $Pn\bar{3}$ structure is also observed (see Figure S2). (d) Valence distribution changes in $PbMO_3$ perovskites. (e) Crystal structures of the phases with a variety of charge distributions expected to appear in $PbCoO_3$ under high-pressure or in chemically modified compounds in high-temperature conditions.

with HSE06) and has previously been used for calculating the electronic properties of a spinel oxide containing mixed-valence Co cations.[35]

3. RESULTS AND DISCUSSION

The product's SXRD pattern (Figure 1a) appeared to be that of a simple cubic perovskite structure ($Pm\bar{3}m$), but the presence of (111) reflection both in the SXRD (inset of Figure 1a) and ED patterns (Figure 1b and S1) revealed the presence of a $2a \times 2a \times 2a$ superlattice, where a is the lattice constant of a simple cubic perovskite. The reflection conditions of $0kl$ ($k + l = 2n$), hhl (any), and $00l$ ($l = 2n$) indicated the $Pn\bar{3}$ space group, the same as that of the low-temperature phase of the quadruple perovskite $CaCu_3Fe_4O_{12}$ ($Ca^{2+}Cu^{2+}_3Fe^{3+}_2Fe^{5+}_2O_{12}$).[36] Rietveld refinement of SXRD data was carried out based on $Pn\bar{3}$ structural model. The A'-site of quadruple perovskites $AA'_3B_4O_{12}$ or $AA'_3B_2B'_2O_{12}$ are generally occupied by Jahn−Teller (JT) active

ions because JT distortion stabilizes the square-planar coordinated A'-site.[36,37] However, several compounds with JT inactive ions (Mn^{2+}, Co^{2+}, and others)[38−40] in the A'-site are reported. These have large atomic displacements of A'-site ions in the direction perpendicular to the A'O_4 square-plane, anisotropic atomic displacement parameters (U_{11}, U_{22} and U_{33}) or splitting of A'-site positions.[38−40] Therefore, anisotropic atomic displacement parameters were applied for the A'-site (6d). The fittings successfully converged. A large value of U_{22} which corresponds to the displacement in the direction perpendicular to the square-planar is consistent with a JT inactive character of a lead. Structure parameters for $Pn\bar{3}$ model and reliability factors of other perovskite model (simple cubic $Pm\bar{3}m$, double perovskite $Fm\bar{3}m$, and quadruple perovskite $Im\bar{3}$) are summarized in Table S1 and S2. It is impossible to accurately refine the oxygen position from SXRD because of the presence of heavy lead atom.

NPD patterns were therefore obtained in order to determine the oxygen position precisely and estimate the valence distribution from bond valence sum (BVS) calculations. Figure 1c shows the result of Rietveld refinement of NPD data collected at room temperature (RT). The structural parameters are summarized in Tables 1 and 2. The oxygen position was

Table 1. Crystallographic Parameters of PbCoO$_3$ at RT Refined from NPD Patterns^a

atoms	site	g	x	y	Z	U_{iso} ($\times 10^{-2}$ Å^2)
Pb1	2a	1	1/2	1/2	1/2	3.44(12)
Pb2	6d	1	1/2	0	0	5.34^b
Co1	4b	1	1/4	1/4	1/4	2.44(44)
Co2	4c	1	3/4	3/4	3/4	3.32(48)
O	24h	1	0.5091(3)	0.2997(2)	0.1960(2)	3.95(4)

^{a}Space group $Pn\overline{3}$ (No. 201), $Z = 2$, $a = 7.64742(3)$ Å, $\rho_{calc} = 9.331(1)$ g/cm^3, $V = 447.245(3)$ Å^3. ^{b}Equivalent isotropic atomic displacement parameters. Anisotropic atomic displacement parameters of Pb2 atom: $U_{11} = 1.76(8) \times 10^{-2}$ Å^2, $U_{22} = 6.40(9) \times 10^{-2}$ Å^2, $U_{33} = 0.86(6) \times 10^{-2}$ Å^2. R values (%): $R_{wp} = 1.78$, $R_B = 4.74$, $\chi^2 = 1.97$.

Table 2. Pb−O and Co−O Bond Lengths and BVSs^a for PbCoO$_3$ at RT

site	Pb1	Pb2	Co1	Co2
M−O bond length (Å)	2.785(3)×12	2.144(3)×4	2.059(3)×6	1.926(3)×6
		2.740(3)×4		
		3.265(3)×4		
BVS	1.95	3.79	2.22	3.26

$^a V_i = \sum_j S_{ij}$, $S_{ij} = \exp\{(r_0 - r_{ij})/0.37\}$. Values calculated using $r_0 = 2.112$ for Pb^{2+}, 2.042 for Pb^{4+}, 1.692 for Co^{2+}, and 1.70 for Co^{3+}.

determined with a satisfactorily small standard deviation. The result of BVS calculations indicated the valence distribution of Pb^{2+}Pb$^{4+}_3$Co$^{2+}_2$Co$^{3+}_2$O$_{12}$ where both Pb and Co have charge orderings in spite of the simple PbCoO$_3$ chemical composition. The average oxidation state is Pb$^{3.5+}$Co$^{2.5+}$O$_3$ with half-integer valences in both A and B sites of the perovskite structure stabilized by the balanced Pb 6s and Co 3d levels, as we expected. The valence distribution of PbMO$_3$ can be controlled according to the depth of the d level of M as schematically illustrated in Figure 1d. No melting of charge orderings was observed when heating PbCoO$_3$ to temperatures below its decomposition temperature (573 K), but considering the valence-skipping nature of Pb and the pressure-induced intermetallic charge transitions observed in BiNiO$_3$[18] and PbCrO$_3$,[22] sequential transitions Pb$^{2+}_{0.25}$Pb$^{4+}_{0.75}$Co$^{2+}_{0.5}$Co$^{3+}_{0.5}$O$_3$ (Pb^{2+}Pb$^{4+}_3$Co$^{2+}_2$Co$^{3+}_2$O$_{12}$) → Pb$^{2+}_{0.25}$Pb$^{4+}_{0.75}$Co$^{2.5+}$O$_3$ → Pb$^{2+}_{0.5}$Pb$^{4+}_{0.5}$Co^{3+}O$_3$ → Pb^{2+}Co^{4+}O$_3$ are expected to occur under pressure as shown in Figure 1e. Substituting other elements for Pb and Co is also expected to stabilize the high-pressure phase and result in heating-induced charge-transfer transitions like those seen in Bi$_{1-x}$Ln$_x$NiO$_3$ and BiNi$_{1-x}$Fe$_x$O$_3$.

The unusual A- and B-site charge orderings were reproduced theoretically by our DFT calculations. We obtained a charge order in 3Pb^{4+}:1Pb^{2+} ratio at the Pb site accompanied by a rocksalt type of Co^{2+}-Co^{3+} charge order at the Co site. The ground-state structure is found to have $R\overline{3}$ symmetry, and is characterized by a slight rhombohedral distortion and antiparallel displacements of Pb cations, in the [001] direction of the
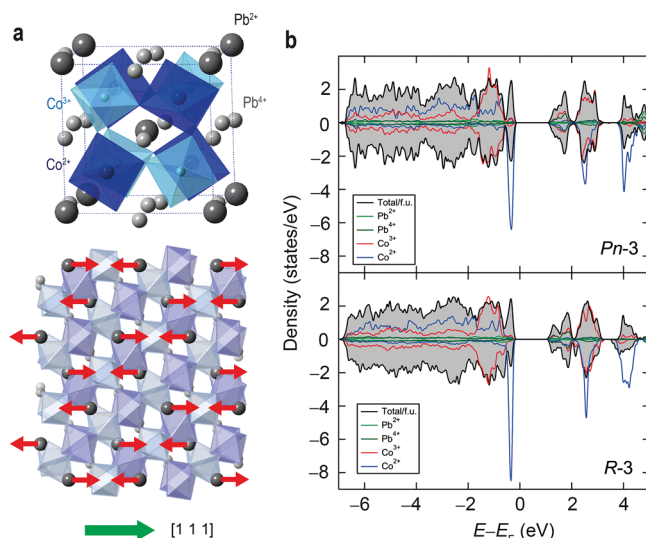
Figure 2. Theoretically predicted ground state structure ($R\overline{3}$) and the corresponding density of states. (a) Pb-cation displacements lower the total energy in the calculated ground state structure. Antiparallel displacements of Pb^{4+} and Pb^{2+} cations are observed in the [001]$_c$ and [111]$_c$ directions, respectively. (b) Calculated total and atom-resolved density of states (DOS) of the calculated antiferromagnetic ground-state structure of PbCoO$_3$. Black lines, total DOS per formula unit; green lines, Pb^{2+} DOS per atom; brown lines, Pb^{4+} DOS per atom; red lines, Co^{3+} DOS per atom; blue lines, Co^{3+} DOS per atom. Two types of both Pb and Co cations are distinguishable.

cubic cell ([001]$_c$) for Pb^{4+} and in the [111]$_c$ direction for Pb^{2+} (see Figure 2a and Table S3), while the experimentally observed cubic phase with $Pn\overline{3}$ symmetry lies 0.06 eV/f.u. higher in energy (see Table S4). The f.u. used in all the calculations was unified to PbCoO$_3$ to compare the energies between different structures. Other calculated structures—$Im\overline{3}$ without Co charge ordering, $Fm\overline{3}m$, and $Pm\overline{3}m$—are all far higher in energy (see Table S5). We speculate that the predicted order of the Pb-cation displacements melted at RT, but the influence may be indirectly observed as the large thermal vibration in A′-site. As shown in Figure 2b, the difference in the two present kinds of both Pb and Co cations is clearly visible in the density of states for both $Pn\overline{3}$ and $R\overline{3}$ structures. Co^{3+} ions were found to be in the low-spin (LS) state, where the t_{2g} orbitals are fully occupied by six electrons; and Co^{2+} ions were found to be in the high-spin (HS) state, where in the majority spin direction all three t_{2g} and the two e_g orbitals are occupied and in the minority spin direction there are only two electrons in the t_{2g} orbitals. The calculated magnetic moment within the Co^{2+} sphere is 2.6 μ_B and the calculated band gap of the $Pn\overline{3}$ phase is 1.35 eV.

To further confirm this unusual valence distribution, Pb-4f HAXPES and Co L-edge XAS measurements were made. The HAXPES results for PbCoO$_3$ and Pb standard materials are shown in Figure 3a, and fitting results are summarized in Table S3. The peak top energies for PbCoO$_3$, 137.44 eV (4f$_{7/2}$) and 142.30 eV (4f$_{5/2}$), are close to those for Pb^{4+}Ni^{2+}O$_3$, indicating that Pb^{4+} is dominant, but the Pb^{2+} contribution less pronounced than that for Pb$^{2+}_{0.5}$Pb$^{4+}_{0.5}$Cr^{3+}O$_3$ is also present. We estimated the fraction of Pb^{2+} from the area ratio of Pb^{2+} and Pb^{4+} contributions by using PbCrO$_3$ data as the standard for Pb$^{2+}_{0.5}$Pb$^{4+}_{0.5}$. The result was Pb$^{2+}_{0.32}$Pb$^{4+}_{0.68}$, in good agreement with the Pb$^{2+}_{0.25}$Pb$^{4+}_{0.75}$ oxidation state indicated by our structural and theoretical studies. The present results indicate that the 4f binding energy of Pb^{2+} is greater than that of Pb^{4+}.
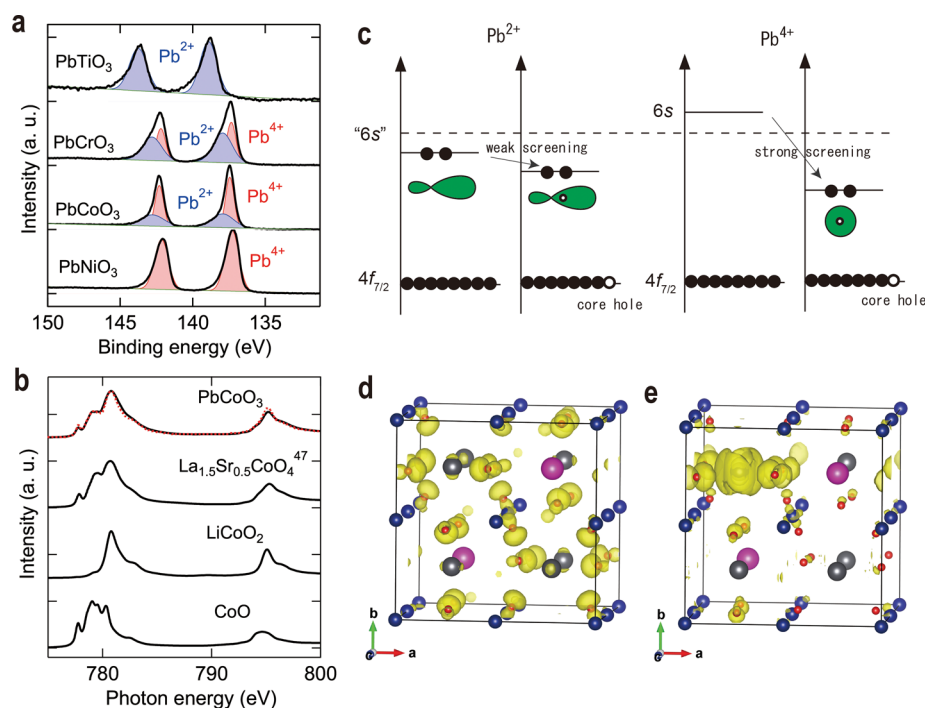
Figure 3. Spectroscopic data confirming the $Pb^{2+}_{0.25}Pb^{4+}_{0.75}Co^{2+}_{0.5}Co^{3+}_{0.5}O_3$ valence distribution of $PbCoO_3$. (a) Pb $4f$ HAXPES results for $PbTiO_3$, $PbCrO_3$, $PbCoO_3$, and $PbNiO_3$ at RT. Predominant Pb^{4+} and the presence of Pb^{2+} are evident in the spectrum for $PbCoO_3$. Fitting results are summarized in Table S6. (b) The Co-$L_{2,3}$ X-ray absorption spectra for $PbCoO_3$ and for CoO and $LiCoO_2$ as a HS Co^{2+} and a LS Co^{3+} references, respectively. The data for $La_{1.5}Sr_{0.5}CoO_4$ is quoted from ref 47 as a $Co^{2.5+}$ reference. The red dotted line represents the sum of CoO and $LiCoO_2$ spectra at a ratio of 0.45:0.55 ($Co^{2.55+}$). (c) Schematic illustration of screening effects of Pb^{2+} and Pb^{4+} cations. The binding energy of Pb^{4+} gets smaller than that of Pb^{2+} because of the strong screening effect. (d) The distribution of the screening charge in the transition-state calculation where half an electron was removed from the $j = 5/2$ $4f$ level of Pb^{2+} in the lower left part of the unit cell; Pb^{2+}, Pb^{4+}, Co, O, and the screening charge are depicted with pink, gray, blue, and red spheres and with yellow clouds, respectively. (e) Same as in (d) but for the $j = 5/2$ $4f$ level of Pb^{4+} in the upper left part of the unit cell. Charge densities were plotted with the aid of VESTA visualization software.[48]

This is opposite to the result of above-mentioned DFT calculation and to a naive expectation that the core levels of the more positive ions have a higher binding energy, but can be understood considering the strong screening effect.

The positively charged core hole created when an electron is ejected from a core level in an HAXPES experiment is screened by the other electrons in the system as schematically illustrated in Figure 3c. This process can be evaluated by DFT calculations using the Slater-Janak transition-state approach,[41,42] where half an electron is removed from the investigated core level and placed into the valence band to calculate the corresponding core-level shift (CLS). Our calculations using this approach showed that the core-level shifts of the Pb^{4+} $4f$ levels are much larger than those of the Pb^{2+} $4f$ levels, yielding the picture observed in our experiment: after the CLS is taken into account, the calculated binding energies of the Pb^{4+} $4f$ levels end up being lower than those of the Pb^{2+} $4f$ levels, by ~0.56 eV for both $j = 5/2$ and $j = 7/2$ states. In order to explain such a large difference in the binding energies of the two cations, it is helpful to plot the distribution of the (screening) charge, which in the transition-state calculation occupies the bottom of the conduction band.[43] This is done in Figure 3d and 3e for the cases when half an electron was removed from the $j = 5/2$ $4f$ levels of Pb^{2+} and Pb^{4+}. The difference in the screening charge distribution is striking. While in the case of the hole in Pb^{2+} core there is no screening charge on Pb^{2+} itself, in the case of the Pb^{4+} core hole the screening charge is almost entirely situated on Pb^{4+} and the neighboring oxygen anions. Such a distribution leads to the "overscreening" observed in our experiment (i.e., to the binding energies of the $4f$ levels of Pb^{2+} appearing to be higher than those

of the $4f$ levels of Pb^{4+}) and is the consequence of the specific electronic density of states of this compound (Figure 2b), where the bottom of the conduction band consists mainly of Pb^{4+} s states hybridized with oxygen p states. It should be noted that in other compounds such as PbO,[44] PbO_2[45] and $Bi_{1-x}Pb_xNiO_3$[46] experiments also yield higher binding energies for the $4f$ levels of Pb^{2+} (Bi^{3+}) and lower ones for Pb^{4+} (Bi^{5+}) ions.

XAS was also used in present work because it is very sensitive to both the valence state and spin state of Co. For comparison, the Co-$L_{2,3}$ XAS of CoO with a HS Co^{2+} state and $LiCoO_2$ with a LS Co^{3+} state were also measured. As shown in Figure 3b, the $PbCoO_3$ spectrum is very similar to that of $La_{1.5}Sr_{0.5}CoO_4$[47] composed of these two references at a ratio of about 1:1. The average valence calculated for the Co in $PbCoO_3$ is close to 2.55, indicating the $Pb^{2+}Pb^{4+}_3Co^{2+}_2Co^{3+}_2O_{12}$ charge combination with HS Co^{2+} and LS Co^{3+} states. The proposed spin states are also in agreement with the theoretical calculation and with the temperature dependence of magnetic susceptibility as discussed later.

The electrical and magnetic properties of $PbCoO_3$ are consistent with $Co^{2+}_{0.5}Co^{3+}_{0.5}$ charge ordering. The semiconducting behavior with a gap of 0.28 eV determined by the Arrhenius plot of resistivity data shown in the inset of Figure 4a is consistent with the rocksalt-type ordering of Co^{2+} (HS) and Co^{3+} (LS). Figure 4b shows the temperature dependence of magnetic susceptibility χ of $PbCoO_3$, measured in a magnetic field of 1 kOe on heating after zero-field cooling. The fitting gives $\chi_0 = 5.5(9) \times 10^{-5}$ emu/mol, $C = 1.365(4)$ emu·K/mol, and $\theta = -17.9(3)$ K. If Co^{3+} is in the nonmagnetic LS state with $S = 0$ as illustrated in Figure 4c, the effective magnetic moment (p_{eff}) per magnetic
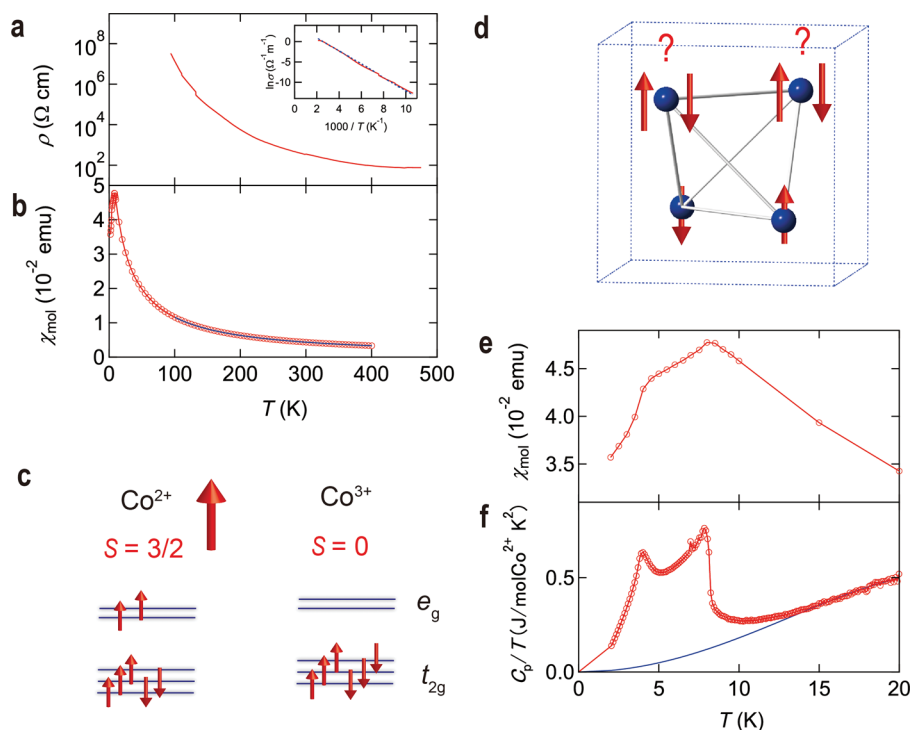
Figure 4. Electrical and magnetic properties of PbCoO$_3$. (a) Temperature dependence of electrical resistivity. The inset shows an Arrhenius plot of the data. PbCoO$_3$ is a semiconductor with band gap of 0.28 eV. (b) Temperature dependence of magnetic susceptibility measured in a magnetic field of 1 kOe on heating after zero-field cooling. The blue line between 100 and 400 K, well above T_N, shows the results of fitting to the Curie–Weiss law with a temperature-independent term χ_0: $\chi = \chi_0 + C/(T - \theta)$, where C is the Curie constant and θ is the Weiss temperature. The inset shows a magnified view of susceptibility near T_N. Two step antiferromagnetic transitions are evident. (c) Spin states of Co^{2+} and Co^{3+} in PbCoO$_3$. Co^{2+} is in a magnetic high-spin state and Co^{3+} is in a nonmagnetic low-spin state. (d) Configuration of magnetic Co^{2+} cations in the $Pn\bar{3}$ perovskite structure. Tetrahedral structure creates geometrical frustration. (e) A magnified view of susceptibility near T_N. Two step antiferromagnetic transitions are evident. (f) Temperature dependence of specific heat divided by temperature. Two step anomalies confirming magnetic orderings at 4.0 and 7.8 K are evident. The blue line is an estimation of the lattice contribution C_L estimated from the data between 20 and 25 K. Its equation is $C_L = \beta_1 T^3 + \beta_2 T^5$, where $\beta_1 = 9.98(10) \times 10^{-4}$ J/molCo^{2+} K^4 and $\beta_2 = -9.40(31) \times 10^{-7}$ J/molCo^{2+} K. This β_1 value gives a Debye temperature of 200 K.

Co^{2+} ion is 4.73 μ_B, which is close to the 4.80 μ_B[49] expected for HS Co^{2+} with $S = 3/2$ identified by the XAS. It should be noted that the relatively small negative Weiss temperature of −17.9 K agrees with above picture because the magnetic interaction is mediated by a Co^{2+}−O−Co^{3+}−O−Co^{2+} path. Magnetic Co^{2+} at the special positions of a cubic cell forms a regular FCC lattice (in other word, tetrahedron as schematically illustrated in Figure 4d) where strong geometrical frustration is expected.[50] Accordingly, the Néel temperature (T_N) is smaller than the absolute value of the Weiss temperature, and unusual two-step transition, one at 4.0 K and the other at 7.8 K, is seen in a magnified view of the temperature dependence of the compound's magnetic susceptibility and specific heat measured in a zero magnetic field (Figure 4e and 4f).

The Pb^{2+}$_{0.25}$Pb^{4+}$_{0.75}$Co^{2+}$_{0.5}$Co^{3+}$_{0.5}$O$_3$ valence distribution in the quadruple perovskite structure Pb^{2+}Pb^{4+}$_3$Co^{2+}$_2$Co^{3+}$_2$O$_{12}$ charge ordered at both A site and B site is thus confirmed. To the best of our knowledge, PbCoO$_3$ is the first example where main group element occupy the A'-site. A large atomic displacement of Pb^{4+} shows the absence of the energy lowering due to the JT distortion, which implies that PbCoO$_3$ has another phase at the HP and HT synthetic condition. PbMO_3 changes with increases in M's atomic number hence in the depth of its d level: from Pb^{2+}M^{4+}O$_3$ (M = Ti or V) to Pb^{2+}$_{0.5}$Pb^{4+}$_{0.5}$$M^{3+}O_3$ (M = Cr or Fe,[51] with an average valence state of Pb^{3+}M^{3+}O$_3$) to Pb^{2+}$_{0.25}$Pb^{4+}$_{0.75}$$M^{2+}$$_{0.5}$$M^{3+}$$_{0.5}O_3$ (M = Co, Pb$^{3.5+}$$M^{2.5+}O_3$), and finally to Pb^{4+}M^{2+}O$_3$ (M = Ni). The only exception is PbMnO$_3$,

which was reported to be Pb^{2+}Mn^{4+}O$_3$[52] despite Mn's atomic number being between those of Cr and Fe both PbCrO$_3$ and PbFeO$_3$ being reported to be Pb^{2+}$_{0.5}$Pb^{4+}$_{0.5}$$M^{3+}O_3$. However, the valence state of PbMnO$_3$ was determined using a sample with significant oxygen deficiency and with the assumption that Pb was divalent. This compound should be reinvestigated using a spectroscopic method and a stoichiometric sample.

4. CONCLUSIONS

We have shown that PbCoO$_3$ has the valence distribution of Pb^{2+}$_{0.25}$Pb^{4+}$_{0.75}$Co^{2+}$_{0.5}$Co^{3+}$_{0.5}$O$_3$ in the quadruple perovskite structure Pb^{2+}Pb^{4+}$_3$Co^{2+}$_2$Co^{3+}$_2$O$_{12}$ charge ordered at both A site and B site. The complex valence distribution is expected to change on perturbations such as pressure and chemical modifications. For example, the melting of Co charge ordering leading to Pb^{2+}$_{0.25}$Pb^{4+}$_{0.75}$Co$^{2.5+}$O$_3$ and intermetallic charge transfer between Pb and Co resulting first in Pb^{2+}$_{0.5}$Pb^{4+}$_{0.5}$Co^{3+}O$_3$ and finally in Pb^{2+}Co^{4+}O$_3$ would be possible under pressure. The investigation of such a rich variety of phases under pressure and the realization in chemically modified PbCoO$_3$ of temperature-change-induced intermetallic charge transfer accompanied by negative thermal expansion as achieved for BiNiO$_3$ and LaCu$_3$Fe$_4$O$_{12}$[53] are big challenges. Finally, we note the present strategy, realizing mixed valence states in both the A and B sites of perovskite compounds by tuning the energy difference between Pb 6s and transition metal 3d orbitals, can be applied to other systems with valence-skipping elements such as Au, Tl, and Sb. Efforts to do so are underway.

■ ASSOCIATED CONTENT

ⓈSupporting Information

The Supporting Information is available free of charge on the ACS Publications website at DOI: 10.1021/jacs.7b01851.

ED patterns along the [011], [001], and [111] zone axis at RT; Magnified view of NPD patterns at RT; Comparison of the reliability factors in the Rietveld analysis of SXRD with respect to the cubic perovskite structures; Structural parameters of $PbCoO_3$ refined from SXRD patterns; Structural parameters of the calculated ground state of $PbCoO_3$ having $R\bar{3}$ and $Pn\bar{3}$ symmetries; Comparison of the energies of several referent structures of $PbCoO_3$; Fitting results for Pb 4f HAXPES of $PbCoO_3$, $PbCrO_3$, $PbNiO_3$, and $PbTiO_3$ (PDF)

■ AUTHOR INFORMATION

Corresponding Authors

*ywlong@iphy.ac.cn
*mazuma@msl.titech.ac.jp

ORCID ⓘ

Ikuya Yamada: 0000-0003-2340-131X
Takashi Mizokawa: 0000-0002-7682-2348
Youwen Long: 0000-0002-8587-7818
Masaki Azuma: 0000-0002-8378-321X

Present Addresses

◀Laboratory for Scientific Developments and Novel Materials, Paul Scherrer Institut, WLGA/U125, 5232 Villigen PSI, Schweiz.
◆Condensed Matter Physics and Materials Science Department, Brookhaven National Laboratory, Upton, New York 11973, United States.
∞Department of Physics and Astronomy, Texas A&M University, College Station, Texas 77843, United States.
◇Department of Energy and Material Science, Kyushu University, Kasuga 816−8580, Japan.
◤Department of Pure and Applied Chemistry, Faculty of Science and Technology, Tokyo University of Science, 2641 Yamazaki, Noda-shi, Chiba 278−8510, Japan.

Notes

The authors declare no competing financial interest.

■ ACKNOWLEDGMENTS

■ REFERENCES

(1) Imada, M.; Fujimori, A.; Tokura, Y. *Rev. Mod. Phys.* **1998**, *70*, 1039−1263.
(2) Radaelli, P. G.; Cox, D. E.; Marezio, M.; Cheong, S. W. *Phys. Rev. B: Condens. Matter Mater. Phys.* **1997**, *55*, 3015−3023.
(3) Attfield, J. P. *Solid State Sci.* **2006**, *8*, 861−867.
(4) Senn, M. S.; Wright, J. P.; Attfield, J. P. *Nature* **2012**, *481*, 173−176.
(5) Ovsyannikov, S. V.; Bykov, M.; Bykova, E.; Kozlenko, D. P.; Tsirlin, A. A.; Karkin, A. E.; Shchennikov, V. V.; Kichanov, S. E.; Gou, H.; Abakumov, A. M.; Egoavil, R.; Verbeeck, J.; McCammon, C.; Dyadkin, V.; Chernyshov, D.; van Smaalen, S.; Dubrovinsky, L. S. *Nat. Chem.* **2016**, *8*, 501−508.
(6) Prodi, A.; Gilioli, E.; Gauzzi, A.; Licci, F.; Marezio, M.; Bolzoni, F.; Huang, Q.; Santoro, A.; Lynn, J. W. *Nat. Mater.* **2004**, *3*, 48−52.
(7) Cava, R. J.; Batlogg, B.; Krajewski, J. J.; Farrow, R.; Rupp, L. W.; White, A. E.; Short, K.; Peck, W. F.; Kometani, T. *Nature* **1988**, *332*, 814−816.
(8) Sleight, A. W.; Gillson, J. L.; Bierstedt, P. E. *Solid State Commun.* **1975**, *17*, 27−28.
(9) Kuwahara, H.; Tomioka, Y.; Asamitsu, Y.; Moritomo, Y.; Tokura, Y. *Science* **1995**, *270*, 961−963.
(10) Terasaki, I.; Sasago, Y.; Uchinokura, K. *Phys. Rev. B: Condens. Matter Mater. Phys.* **1997**, *56*, R12685.
(11) Dismukes, G. C.; Siderer, Y. *Proc. Natl. Acad. Sci. U. S. A.* **1981**, *78*, 274−278.
(12) Lelmini, D.; Waser, R. *Resistive Switching: From Fundamentals of Nanoionic Redox Processes to Memristive Device Applications*; Wiley-VCH Verlag GmbH & Co. KGaA: Weinheim, 2016.
(13) Cox, D. E.; Sleight, A. W. *Acta Crystallogr., Sect. B: Struct. Crystallogr. Cryst. Chem.* **1979**, *35*, 1−10.
(14) Harrison, W. A. *Phys. Rev. B: Condens. Matter Mater. Phys.* **2006**, *74*, 245128.
(15) Bode, H. *Lead-Acid Batteries*; John Wiley and Sons, Inc.: New York, 1977.
(16) Naka, M.; Seo, H.; Motome, Y. *Phys. Rev. Lett.* **2016**, *116*, 056402.
(17) Ishiwata, S.; Azuma, M.; Takano, M.; Nishibori, E.; Takata, M.; Sakata, M.; Kato, K. *J. Mater. Chem.* **2002**, *12*, 3733−3737.
(18) Azuma, M.; Chen, W. T.; Seki, H.; Czapski, M.; Olga, S.; Oka, K.; Mizumaki, M.; Watanuki, T.; Ishimatsu, N.; Kawamura, N.; Ishiwata, S.; Tucker, M. G.; Shimakawa, Y.; Attfield, J. P. *Nat. Commun.* **2011**, *2*, 347.
(19) Oka, K.; Nabetani, K.; Sakaguchi, C.; Seki, H.; Czapski, M.; Shimakawa, Y.; Azuma, M. *Appl. Phys. Lett.* **2013**, *103*, 061909.
(20) Nabetani, K.; Muramatsu, Y.; Oka, K.; Nakano, K.; Hojo, H.; Mizumaki, M.; Agui, A.; Higo, Y.; Hayashi, N.; Takano, M.; Azuma, M. *Appl. Phys. Lett.* **2015**, *106*, 061912.
(21) Belik, A. A.; Azuma, M.; Saito, T.; Shimakawa, Y.; Takano, M. *Chem. Mater.* **2005**, *17*, 269−273.
(22) Yu, R.; Hojo, H.; Watanuki, T.; Mizumaki, M.; Mizokawa, T.; Oka, K.; Kim, H.; Machida, A.; Sakaki, K.; Nakamura, Y.; Agui, A.; Mori, D.; Inaguma, Y.; Schlipf, M.; Rushchanskii, K. Z.; Ležaić, M.; Matsuda, M.; Ma, J.; Calder, S.; Isobe, M.; Ikuhara, Y.; Azuma, M. *J. Am. Chem. Soc.* **2015**, *137*, 12719−12728.
(23) Inaguma, Y.; Tanaka, K.; Tsuchiya, T.; Mori, D.; Katsumata, T.; Ohba, T.; Hiraki, K. I.; Takahashi, T.; Saitoh, H. *J. Am. Chem. Soc.* **2011**, *133*, 16920−16929.
(24) Izumi, F.; Momma, K. *Solid State Phenom.* **2007**, *130*, 15−20.
(25) Oishi, R.; Yonemura, M.; Nishimaki, Y.; Torii, S.; Hoshikawa, A.; Ishigaki, T.; Morishima, T.; Mori, K.; Kamiyama, T. *Nucl. Instrum. Methods Phys. Res., Sect. A* **2009**, *600*, 94−96.

(26) Oishi-Tomiyasu, R.; Yonemura, M.; Morishima, T.; Hoshikawa, A.; Torii, S.; Ishigaki, T.; Kamiyama, T. *J. Appl. Crystallogr.* **2012**, *45*, 299−308.

(27) Ueda, S.; Katsuya, Y.; Tanaka, M.; Yoshikawa, H.; Yamashita, Y.; Ishimaru, S.; Matsushita, Y.; Kobayashi, K. *AIP Conf. Proc.* **2009**, *1234*, 403−406.

(28) Ueda, S. *J. Electron Spectrosc. Relat. Phenom.* **2013**, *190*, 235−241.

(29) Kresse, G.; Furthmüller, J. *Phys. Rev. B: Condens. Matter Mater. Phys.* **1996**, *54*, 11169−11186.

(30) Blöchl, P. E. *Phys. Rev. B: Condens. Matter Mater. Phys.* **1994**, *50*, 17953−17979.

(31) Krukau, A. V.; Vydrov, O. A.; Izmaylov, A. F.; Scuseria, G. E. *J. Chem. Phys.* **2006**, *125*, 224106.

(32) Franchini, C. *J. Phys.: Condens. Matter* **2014**, *26*, 253202.

(33) The Juelich FLEUR project Home Page, http://www.flapw.de/pm/index.php (accessed Feb 24, 2017).

(34) Perdew, J. P.; Burke, K.; Ernzerhof, M. *Phys. Rev. Lett.* **1996**, *77*, 3865.

(35) Chen, J.; Wu, X.; Selloni, A. *Phys. Rev. B: Condens. Matter Mater. Phys.* **2011**, *83*, 245204.

(36) Yamada, I.; Takata, K.; Hayashi, N.; Shinohara, S.; Azuma, M.; Mori, S.; Muranaka, S.; Shimakawa, Y.; Takano, M. *Angew. Chem., Int. Ed.* **2008**, *47*, 7032−7035.

(37) Collomb, A.; Samaras, D.; Chenavas, J.; Marezio, M.; Joubert, J. C.; Bochu, B.; Deschizeaux, M. N. *J. Magn. Magn. Mater.* **1978**, *7*, 1−8.

(38) Shimura, G.; Niwa, K.; Shirako, Y.; Muto, S.; Kusaba, K. *Solid State Commun.* **2016**, *234−235*, 40−44.

(39) Ovsyannikov, S. V.; Zainulin, Y. G.; Kadyrova, N. I.; Tyutyunnik, A. P.; Semenova, A. S.; Kasinathan, D.; Tsirlin, A. A.; Miyajima, N.; Karkin, A. E. *Inorg. Chem.* **2013**, *52*, 11703−11710.

(40) Tohyama, T.; Senn, M. S.; Saito, T.; Chen, W.; Tang, C. C.; Attfield, J. P.; Shimakawa, Y. *Chem. Mater.* **2013**, *25*, 178−183.

(41) Janak, J. F. *Phys. Rev. B: Condens. Matter Mater. Phys.* **1978**, *18*, 7165−7168.

(42) Slater, J. C. *Quantum Theory of Molecules and Solids*; McGraw-Hill: New York, 1974; International Series in Pure and Applied Physics, Vol. 4.

(43) Olovsson, W.; Göransson, C.; Marten, T.; Abrikosov, I. A. *Phys. Status Solidi B* **2006**, *243*, 2447−2464.

(44) Rondon, S.; Sherwood, P. M. A. *Surf. Sci. Spectra* **1998**, *5*, 104−110.

(45) Rondon, S.; Sherwood, P. M. A. *Surf. Sci. Spectra* **1998**, *5*, 97−103.

(46) Nakano, K.; Oka, K.; Watanuki, T.; Mizumaki, M.; Machida, A.; Agui, A.; Kim, H.; Komiyama, J.; Mizokawa, T.; Nishikubo, T.; Hattori, Y.; Ueda, S.; Sakai, Y.; Azuma, M. *Chem. Mater.* **2016**, *28*, 6062−6067.

(47) Chang, C. F.; Hu, Z.; Wu, H.; Burnus, T.; Hollmann, N.; Benomar, M.; Lorenz, T.; Tanaka, A.; Lin, H. J.; Hsieh, H. H.; Chen, C. T.; Tjeng, L. H. *Phys. Rev. Lett.* **2009**, *102*, 116401.

(48) Momma, K.; Izumi, F. *J. Appl. Cryst.* **2008**, *41*, 653−658.

(49) Ashcroft, N. W.; Mermin, N. D. *Solid State Physics*; Harcourt College Publishers: Fort Worth, 1976.

(50) Ramirez, A. P. *Annu. Rev. Mater. Sci.* **1994**, *24*, 453−480.

(51) Tsuchiya, T.; Saito, H.; Yoshida, M.; Katsumata, T.; Ohba, T.; Inaguma, Y.; Tsurui, T.; Shikano, M. *Mater. Res. Soc. Symp. Proc.* **2006**, *988E*, 0988−QQ06−03.

(52) Oka, K.; Azuma, M.; Hirai, S.; Belik, A. A.; Kojitani, H.; Akaogi, M.; Takano, M.; Shimakawa, Y. *Inorg. Chem.* **2009**, *48*, 2285−2288.

(53) Long, Y. W.; Hayashi, N.; Saito, T.; Azuma, M.; Muranaka, S.; Shimakawa, Y. *Nature* **2009**, *458*, 60−63.